Nanoscale

PAPER

View Article Online
View Journal | View Issue



Cite this: *Nanoscale*, 2026, **18**, 3941

# Multifunctional nonlinear photonic devices based on spatial self-phase modulation in InP nanosheets

Danyi Weng,[a] Cheng Ling,[a] Jun He,[b] Qiannan Cui, *[a] Chunxiang Xu *[a] and Bing Gu *[a]

Received 20th October 2025,
Accepted 8th January 2026

DOI: 10.1039/d5nr04405g

rsc.li/nanoscale

Indium phosphide (InP) has high carrier mobility and excellent optoelectronic properties, demonstrating significant potential for applications in optical communications and photodetectors. Its two-dimensional (2D) nanosheets exhibit unique optical nonlinearity due to quantum confinement effects, yet their third-order nonlinear optical properties remain rarely explored. In this work, we prepare and characterize InP nanosheet dispersions, investigate their spatial self-phase modulation (SSPM) behaviors, and demonstrate their applications in multifunctional nonlinear photonic devices. By studying the ring formation dynamics of SSPM patterns, the ring formation time $\tau_F$ and the third-order nonlinear susceptibility of monolayer InP nanosheets $\chi^{(3)}_{monolayer}$ are found to be about 0.3 s and $10^{-9}$ esu, respectively. The formation mechanism of SSPM primarily arises from the interaction between coherent light and InP nanosheets. Leveraging the superior electronic coherence and photostability of InP nanosheets, four types of nonlinear photonic devices are designed and demonstrated, including all-optical switches, spatially asymmetric light transmitters, photonic diodes, and optical logic gates. This work not only bridges a critical gap in the third-order nonlinear optical research of III–V semiconductor nanomaterials but also opens new avenues for developing high-performance multifunctional nonlinear photonic devices.



## 1 Introduction

Over the past two decades, III–V compound semiconductors have shown tremendous application prospects in developing high-performance optoelectronic devices, such as lasers,[1] photodetectors,[2] modulators,[3] solar cells,[4] light-emitting diodes,[4] and single-photon emitters,[5] owing to their unique electrical and optical properties.[6] Among them, indium phosphide (InP) is an extremely attractive direct-bandgap III–V semiconductor with an ultra-high electron mobility of 4800 $cm^2\ V^{-1}\ s^{-1}$ at room temperature,[7] which is approximately three times that of silicon (1450 $cm^2\ V^{-1}\ s^{-1}$).[8] This characteristic endows it with exceptional applications in near-infrared band optoelectronic devices. For instance, Chen *et al.*[9] employed a Zn diffusion technique to achieve high responsivity in planar InP/InGaAs/InP photodetectors at 1310 nm and 1550 nm. Jain *et al.*[10] developed avalanche photodetectors based on InP/InAsP nanowires, exhibiting 12-fold gain at 1550 nm. Recently, Zhang *et al.*[11] reported superior electrical performance in InGaAs/InP photodetectors and investigated their charge transport processes.

Beyond its exceptional optoelectronic properties, InP's remarkable nonlinear optical properties have also attracted significant research interest. As early as 1995, Dvorak *et al.*[12] characterized the nonlinear refractive index (~$10^{-12}$ $cm^2\ W^{-1}$) of bulk InP at 1064 nm using *Z*-scan measurements. In 2007, Wang *et al.*[13] demonstrated that InP nanocrystals exhibit strong nonlinear optical properties, with a nonlinear refractive index (~$10^{-9}$ $cm^2\ W^{-1}$) three orders of magnitude greater than that of bulk InP. Most recently in 2020, Liu *et al.*[6] reported superior nonlinear absorption properties of InP nanowires and their application as saturable absorbers for ultrafast laser pulse generation. In short, InP nanostructures exhibit diverse forms, including nanocrystals, nanowires, and nanosheets. It is well documented that the optical nonlinearity of InP strongly depends on its nano-structural configuration.[6,13] Notably, two-dimensional (2D) nanosheets—owing to their quantum confinement effects—localize electrons within the planar dimension, manifesting unique optical nonlinearity.[14] However, studies on third-order nonlinear optical effects in InP nanosheets remain rarely reported to date.

Spatial self-phase modulation (SSPM) refers to a phenomenon where an intense laser beam transmitted through a third-order nonlinear optical sample generates concentric

[a]*School of Electronic Science & Engineering, Southeast University, Nanjing 211198, China. E-mail: qiannan@seu.edu.cn, xcxseu@seu.edu.cn, gubing@seu.edu.cn*
[b]*School of Physics and Electronics, Central South University, Changsha 410012, China*

multi-ring patterns in the far field.[15,16] Due to its simple experiments, intuitive results, and convenient calculations, SSPM has emerged as a prevalent technique for characterizing the nonlinear optical properties of emerging 2D nanomaterials, including violet phosphorus (VP),[17] SnS,[18] graphene oxide (GO),[19] $Ti_3C_2T_x$,[20] and $Ga_2Te_3$.[21] Meanwhile, SSPM based on novel materials has enabled the development of diverse passive nonlinear photonic devices, such as all-optical switches,[14] photonic diodes,[22] optical isolators,[23] information converters,[18] logic gates,[24] spatially asymmetric light transmitters,[25] *etc*. Specifically, Wu *et al.*[14] reported a dual-wavelength all-optical switch using $MoS_2$ nanosheets. Nayak *et al.*[26] demonstrated all-optical modulations and photonic diodes based on SSPM in porphyrin–naphthalimide molecules. Weng *et al.*[25] developed both spatially asymmetric light propagation and all-optical switching based on the SSPM of semimetal MoP microparticles. Wu *et al.*[23] designed all-optical logic OR gates and optical isolators using a 1D@0D hybrid heterojunction. Notably, Xu *et al.*[24] ingeniously constructed an integrated and reconfigurable multifunctional all-optical logic gate, achieving nine basic Boolean logic functions in a single configuration. In a word, researchers have developed single- or dual-function nonlinear photonic devices based on the excellent SSPM of diverse nanomaterials. Nevertheless, with the continuous emergence of novel optical materials, traditional single-function devices fail to meet the demand for integration and multifunctionality in future intelligent photonic chips. Consequently, there is an urgent need to develop multifunctional nonlinear photonic devices based on unified material platforms—for instance, utilizing SSPM in a single material to simultaneously achieve all-optical switching, wavelength conversion, and logic gates—thereby overcoming current device limitations and advancing next-generation photonic integration technologies.

In this work, we prepared InP nanosheets, studied their SSPM phenomena, and demonstrated their multifunctional nonlinear photonic device applications. By measuring the ring formation dynamics of SSPM patterns, the ring formation time $\tau_F$ and the third-order nonlinear susceptibility of monolayer InP nanosheets $\chi^{(3)}_{monolayer}$ were obtained, and the underlying SSPM formation mechanism was analyzed. Furthermore, leveraging the superior electronic coherence and photostability of InP nanosheets, four types of nonlinear photonic devices were designed and demonstrated, including all-optical switches using InP nanosheets, spatially asymmetric light transmitters in InP/GO, photonic diodes using InP/$SnS_2$, and optical logic gates based on InP nanosheets.

# 2 Preparation and characterization of InP nanosheets

## 2.1 Preparation of InP nanosheets

In the presented work, all samples were prepared using the ultrasonic method, known for its simplicity and widespread application, which facilitates the large-scale exfoliation and dispersion of 2D nanomaterials in solvents.[27] Bulk InP was purchased from Meryer (Shanghai) Biochemical Technology Co., Ltd as the raw material. The bulk InP was ground and sieved and then 60 mg of the processed material was ultrasonically treated for 450 min in 30 mL of 1-methyl-2-pyrrolidone (NMP) solution. During the entire ultrasound process, the temperature was maintained below 30 °C to prevent material oxidation. After standing for 12 hours, the resulting dark gray suspension separated into two distinct layers: the supernatant and the precipitate. The supernatant was collected for subsequent material characterization and SSPM measurements. To determine the mass concentration $d_0$ of the supernatant, the precipitate was rinsed and dried at 85 °C for 10 hours. After weighing, 56.2 mg of InP was obtained, thereby revealing that the supernatant contained 3.8 mg of InP. Therefore, the mass concentration of InP nanosheets dispersed in NMP solution was calculated to be $d_0 = 0.127$ mg mL$^{-1}$.

## 2.2 Material characterization

To characterize the as-prepared InP nanosheets, we conducted the following analyses: the morphology was characterized using a Zeiss GeminiSEM 360 scanning electron microscope (SEM); the crystal structure was determined using a Rigaku Smartlab 9 X-ray diffractometer (XRD); the molecular vibration signatures were recorded using a Horiba Scientific LabRAM HR Evolution Raman spectrometer; the topography and thickness distribution were mapped using a Bruker Dimension Icon atomic force microscope (AFM); and the linear absorption spectrum of InP nanosheets in NMP solution was measured employing a Shimadzu 3600 Plus UV-Vis-NIR spectrophotometer.

## 2.3 Characterization results

Fig. 1(a) shows the SEM image of the as-prepared InP nanosheets, which indicates that a larger number of InP crystals are successfully exfoliated into nanosheets *via* the ultrasonic method. As shown in Fig. 1(b), the XRD pattern of InP nanosheets exhibits three prominent diffraction peaks at $2\theta$ = 26.2°, 43.5°, and 51.5°, indexed to the (111), (220), and (311) planes of the zinc blende-structured InP (reference PDF #73-1983),[28] confirming the typical zinc blende crystal of the as-prepared samples. The significantly reduced peak intensity at $2\theta$ = 26.2° can be attributed to the decrease in crystallinity of the nanosheets. Fig. 1(c) displays the Raman spectrum of InP nanosheets. Two distinct characteristic peaks are observed at 304 cm$^{-1}$ and 344 cm$^{-1}$, which are assigned to the transverse optical and longitudinal optical modes, respectively. It is noteworthy that the transverse optical peak position of the InP nanosheets coincides with that of InP nanowires, while the longitudinal optical peak is completely consistent with that of bulk InP.[29] Fig. 1(d) and (e) present the AFM image of InP nanosheets and the corresponding thickness distribution statistics, respectively. Since the influence of SSPM is almost independent of the lateral size of the 2D nanosheets,[17–20] here we only focus on the thickness of InP nanosheets. Analysis of the red Gaussian fitting curve in Fig. 1(e) yields an average nanosheet thickness of 2.1 nm. This value corresponds to the

 

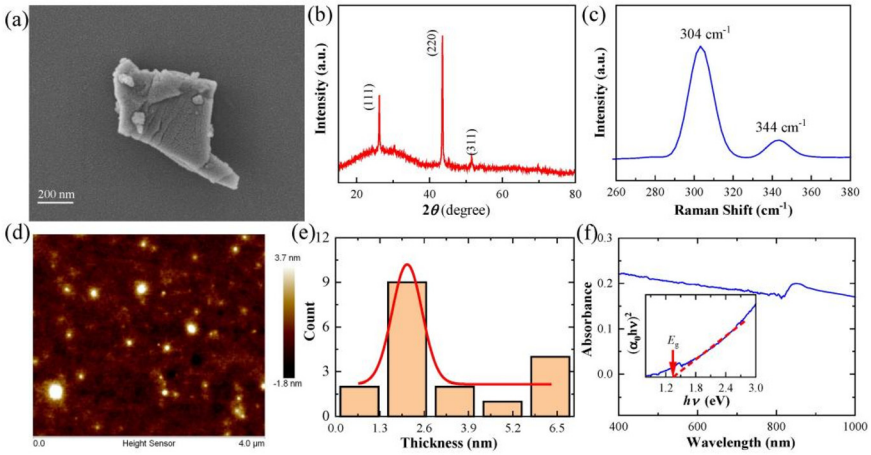


**Fig. 1** Characterization of InP nanosheets. (a) SEM image, (b) XRD pattern, and (c) Raman spectrum of the as-prepared InP nanosheets. (d) AFM image of InP nanosheets with (e) the corresponding thickness distribution statistics. (f) UV-Vis-IR absorption spectrum of InP nanosheets in NMP solution; the inset is $(\alpha_0 h\nu)^2$ *versus* $h\nu$.

theoretical thickness of monolayer InP nanosheets and shows excellent agreement with literature reports.[17] Fig. 1(f) shows the UV-Vis-NIR absorption spectrum of InP nanosheets in NMP solution, revealing weak absorption across the broad spectral range. The optical bandgap of InP nanosheets is determined as $E_g$ = 1.38 eV using Tauc's formula $(\alpha_0 h\nu)^2 = \text{const}\ (h\nu - E_g)$,[30] where $\alpha_0$ denotes the linear absorption coefficient and $h\nu$ represents the photon energy. The inset in Fig. 1(f) presents the corresponding Tauc plot, demonstrating the linear relationship between $(\alpha_0 h\nu)^2$ and $h\nu$. The $E_g$ value is found to be 1.38 eV, which is in close agreement with reported ones.[31,32]

# 3 Nonlinear optical properties of InP nanosheets

## 3.1 SSPM experiments

Based on the advantages of simple experiments, intuitive results, and convenient calculations, SSPM has been extensively employed for characterizing the third-order nonlinear refractive index of diverse nanomaterials.[15,16] In the SSPM experiments, two different wavelengths of fundamental Gaussian laser beams with wavelengths of $\lambda$ = 532 nm (green light) and $\lambda$ = 671 nm (red light) serve as light sources. The nonlinear optical sample consists of InP nanosheets with a mass concentration of $d_0$ = 0.127 mg mL$^{-1}$ dispersed in NMP solution and placed in a quartz cuvette with a thickness of $L$ = 10 mm. The combination of a half-wave plate and a Glan–Taylor prism (G–T) is used to precisely control the laser power incident on the sample. The laser beam is focused onto the sample through a convex lens with a focal length of $f$ = 400 mm, and its waist radii on the focal plane are estimated to be 77.0 μm at $\lambda$ = 532 nm and 68.9 μm at $\lambda$ = 671 nm, respectively. The back surface of the cuvette is positioned 30 mm before the focal plane. Ultimately, the formation dynamics of the self-diffraction ring patterns could be monitored on a white screen or a camera located 150 mm from the back surface of the sample.

## 3.2 Formation dynamics of SSPM

In the SSPM experiment, we recorded the dynamic evolution of the far-field self-diffraction ring of InP nanosheets dispersed in NMP solution at different intensities $I$ with respect to the laser irradiation time $t$ (defined as the time delay at the start of laser irradiation). Fig. 2(a) displays the evolution of a representative self-diffraction ring pattern over time $t$ at $I$ = 205.5 W cm$^{-2}$. It is shown that the dynamic formation process of SSPM rings can be decoupled into three stages, namely (i) ring growth stage: the initial circular spot evolves into a concentric multi-ring structure, the ring size continues to expand and the number of rings increases until a complete self-diffraction ring is formed, at which time the number of self-diffraction rings reaches its maximum $N_{max}$ and the outermost ring radius reaches its maximum $R_{max}$; (ii) ring collapse stage: under the influence of gravity-driven thermal convection, the upper half of the complete self-diffraction ring collapses towards the center; and (iii) steady state stage: the distorted ring structure approaches a time-invariant steady state. This dynamic process can quantify two characteristic time parameters: (i) the ring formation time $\tau_F$, which is defined as the time interval from the start of laser irradiation to the formation of a complete self-diffraction ring and (ii) the ring collapse time $\tau_C$, which is the time interval between the complete self-diffraction ring evolving into a steady-state distorted ring. As shown in Fig. 2(a), we achieved the maximum number of rings $N_{max}$ = 14, the ring formation time $\tau_F$ = 0.32 s, and the ring collapse time $\tau_C$ = 1.21 s for the InP nanosheets dispersed in NMP solution at $I$ = 205.5 W cm$^{-2}$. The measured $\tau_F$ value is comparable to those of ~0.37 s of VP nanosheets[17] and ~0.38 s of MoP microparticles.[25]

Fig. 2(b) shows the evolution of the number of self-diffraction rings $N$ over time $t$ at three representative intensities of $I$ =

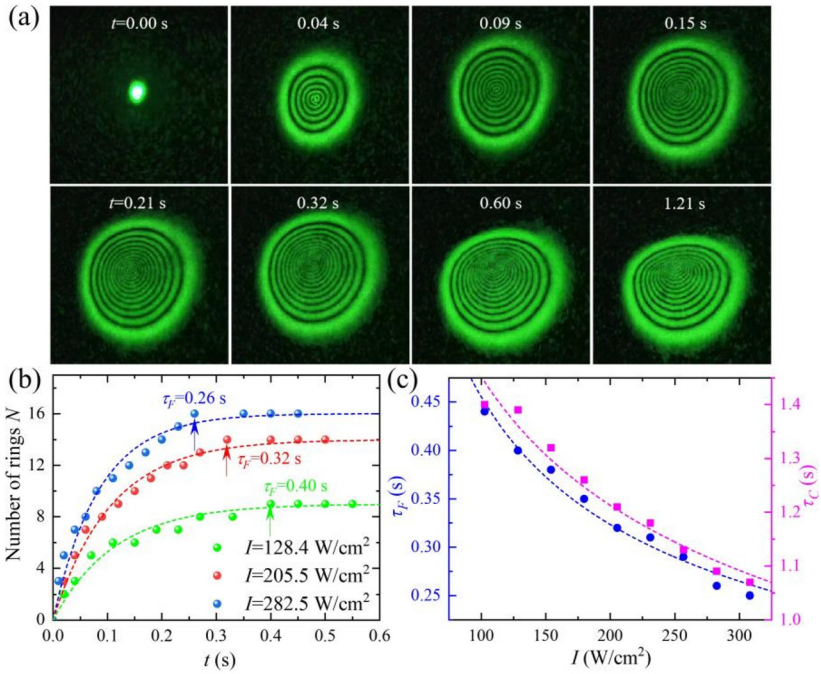


**Fig. 2** Dynamics of ring formation in SSPM patterns. (a) The SSPM patterns of InP nanosheets dispersed in NMP at different times $t$ with $I$ = 205.5 W cm$^{-2}$. (b) The evolution of the ring number $N$ over time $t$ at three representative intensities $I$. (c) The formation time $\tau_F$ and the collapse time $\tau_C$ of the ring at different intensities $I$.

128.4, 205.5, and 282.5 W cm$^{-2}$. The experimental results show that the number of rings $N$ increases nonlinearly with time $t$ and gradually saturates, eventually approaching a constant value. This dynamic behavior is governed by $N(t) = N_{max}[1 - \exp(-t/\tau_R)]$, where $\tau_R$ denotes the characteristic rise time for self-diffraction ring formation. In Fig. 2(b), the dashed lines represent the optimal fitting curves of the measured $N(t) - t$ data, from which the characteristic rise time $\tau_R$ at intensities $I$ = 128.4, 205.5, and 282.5 W cm$^{-2}$ are obtained as 0.113, 0.106, and 0.084 s, respectively. Concurrently, the ring formation times $\tau_F$ measured at $I$ = 128.4, 205.5, and 282.5 W cm$^{-2}$ are 0.40, 0.32, and 0.26 s, respectively. Fig. 2(c) presents the dependence of both the ring formation time $\tau_F$ and the ring collapse time $\tau_C$ on the laser intensity $I$. It is shown that the experimentally measured $\tau_F$ values exhibit an inverse proportionality to the intensity $I$, consistent with previous reports.[14,17,25,33,34] Similarly, the measured $\tau_C$ values are also inversely proportional to the intensity $I$. The above phenomenon can be recapitulated as follows: the higher the intensity, the faster the nonlinear optical response, resulting in a significant reduction in the formation time of self-diffraction rings and thereby a markedly accelerated collapse process. Next, the physical mechanism behind this phenomenon will be described in detail.

### 3.3 Formation mechanism of SSPM

The formation dynamics of SSPM in InP nanosheet suspensions originates from the physical mechanism of coherent light–nanosheet interactions, which we briefly analyze below. The optical bandgap of InP nanosheets is $E_g$ = 1.38 eV, while the incident photon energy $h\nu$ = 2.33 eV at $\lambda$ = 532 nm or 1.85 eV at 671 nm in the experiments resides in the non-parabolic region of their band structure. Owing to the high electron mobility of InP up to 4800 cm$^2$ V$^{-1}$ s$^{-1}$ at room temperature,[7,35] intense laser irradiation induces a significant population of valence-band electrons in the InP nanosheets to absorb photons and undergo transitions to the conduction band. Driven by the optical electric field, the intense laser beam induces polarization and reorientation of InP nanosheets dispersed in NMP solution through an energy-relaxation mechanism. The coherent interplay between the Gaussian beam and the reoriented InP nanosheets enhances the phase modulation effect, leading to a progressive increase in the self-diffraction ring number over time (see Fig. 2(a)). Within this process, the SSPM phenomenon originates from non-local electron coherent interaction between the incident laser beam and the InP nanosheets. The formation dynamics of SSPM in the NMP-suspended InP nanosheets can be physically interpreted using the wind-chime model.[14] Beyond the laser-induced electron coherence that dominates the formation of self-diffraction ring patterns, the thermal effect also contributes partially to the SSPM process—as evidenced by the collapse of the upper self-diffraction ring segment at $t$ = 0.60 s, as shown in Fig. 2(a), which arises from gravity-driven thermal convection in the solution. Consequently, the primary physical origin of light–InP interactions in the SSPM phenomenon is laser-induced electron coherence, with the thermal effect constituting a secondary contribution.

 

### 3.4 Nonlinear optical characterization of InP suspensions

At a fixed laser intensity, the SSPM ring formation dynamics yield a complete self-diffraction ring pattern (*e.g.*, Fig. 2(a)), enabling measurement of the maximum number of rings $N_{max}$. By systematically varying the intensity $I$ and repeating the SSPM experiments, we obtain the $N_{max}$ values across different intensities at 532 nm and 671 nm wavelengths, with the results presented in Fig. 3(a) and (b). Note that we repeat each SSPM experiment three times and obtain similar experimental results, which proves the reliability of the measurement results. Correspondingly, the insets in Fig. 3(a) and (b) display complete self-diffraction ring patterns at two characteristic intensities.

Quantitatively, the intensity-dependent maximum ring number $N_{max}$ follows a linear relationship $N_{max} = sI$, where $s$ is the proportionality coefficient. The dashed lines in Fig. 3 represent the optimal linear fits to the $N_{max} - I$ data, yielding $s$ = 0.061 ± 0.001 and 0.026 ± 0.001 cm$^2$ W$^{-1}$ at 532 nm and 671 nm, respectively. Using the measured $s$ values, the nonlinear refractive indices $n_2$ of InP nanosheet suspensions can be directly determined by:[36,37]

$$n_2 = \frac{\lambda}{2n_0L_{eff}}s, \quad (1)$$

where $n_0$ and $L_{eff} = [1 - \exp(-\alpha_0 L)]/\alpha_0$ are the linear refractive index and the effective thickness of the sample, respectively. Given the diluted InP nanosheets in NMP solvent (*e.g.*, the mass concentration of $d_0$ = 0.127 mg mL$^{-1}$), the linear refractive index $n_0$ of the dispersion approximates that of pure NMP solvent. Thus, we assign $n_0$ = 1.468.

Based on the measured $s$ values from Fig. 3 and the known experimental parameters (*e.g.*, $L_{eff}$ = 9.409 mm at $\lambda$ = 532 nm), eqn (1) yields the nonlinear refractive indices $n_2 = (1.18 \pm 0.02) \times 10^{-6}$ cm$^2$ W$^{-1}$ at 532 nm and $(6.92 \pm 0.08) \times 10^{-7}$ cm$^2$ W$^{-1}$ at 671 nm. For comparison, Table 1 summarizes the nonlinear refractive indices $n_2$ of representative nanosheet suspensions. Clearly, the $n_2$ values of InP nanosheets dispersed in NMP are comparable to or superior to those of VP nanosheets in NMP ($n_2 = 1.87 \times 10^{-6}$ cm$^2$ W$^{-1}$ at 532 nm and $5.58 \times 10^{-7}$ cm$^2$ W$^{-1}$ at 671 nm),[33] the 2D $Ga_2Te_3$ suspension ($2.60 \times 10^{-7}$ cm$^2$ W$^{-1}$ at 532 nm),[21] and the suspended $MoSe_2$ nanoflakes ($6.60 \times 10^{-6}$ cm$^2$ W$^{-1}$ at 671 nm).[34]

Table 1 Nonlinear refractive index $n_2$ and third-order nonlinear susceptibility $\chi^{(3)}_{monolayer}$ of representative 2D nanomaterials at 532 nm and 671 nm wavelengths

| Wavelength | Sample | $n_2$ (cm$^2$ W$^{-1}$) | $\chi^{(3)}_{monolayer}$ (esu) | Ref. |
|---|---|---|---|---|
| 532 nm | VP | $1.87 \times 10^{-6}$ | $1.08 \times 10^{-8}$ | 33 |
| | $Ga_2Te_3$ | $2.60 \times 10^{-7}$ | $1.12 \times 10^{-9}$ | 21 |
| | SnS | $4.53 \times 10^{-5}$ | $7.00 \times 10^{-10}$ | 18 |
| | InP | $1.18 \times 10^{-6}$ | $1.28 \times 10^{-9}$ | This work |
| 671 nm | VP | $5.58 \times 10^{-7}$ | $3.23 \times 10^{-9}$ | 33 |
| | $MoSe_2$ | $6.60 \times 10^{-6}$ | $1.35 \times 10^{-8}$ | 34 |
| | InSe | $5.50 \times 10^{-6}$ | $2.87 \times 10^{-10}$ | 38 |
| | InP | $6.92 \times 10^{-7}$ | $7.52 \times 10^{-10}$ | This work |

### 3.5 Third-order nonlinear susceptibility of monolayer InP nanosheets

The measured $n_2$ reflects contributions from the multilayer InP nanosheets in the dispersion, and its value is directly related to the thickness of the cuvette, the concentration of the dispersion, and other factors. Therefore, it is necessary to extract the third-order nonlinear susceptibility $\chi^{(3)}_{monolayer}$ of monolayer nanosheets. The third-order nonlinear susceptibility $\chi^{(3)}_{monolayer}$ of monolayer InP nanosheets can be calculated by:[37]

$$\chi^{(3)}_{monolayer}(esu) = \frac{{n_0}^2 n_2(cm^2\,W^{-1})}{0.0395 \times {N_{eff}}^2}, \quad (2)$$

where $N_{eff}$ represents the effective number of InP nanosheet layers that the laser beam passes through the cuvette. Here, the solution concentration method is used to estimate the $N_{eff}$ value,[14] and the calculation process is as follows. The InP nanosheet dispersion with a mass concentration of $d_0$ = 0.127 mg mL$^{-1}$ (alternatively, a molar concentration of $\rho = 8.7 \times 10^{-4}$ mol L$^{-1}$) is placed in the cuvette with a volume of $V$ = 3 mL, so that the total number of original cells of InP nanosheets in the cuvette is calculated as $M = (\rho/8) \times V \times N_A = 1.96 \times 10^{17}$, where $N_A$ is Avogadro's constant. Furthermore, since InP crystallizes in the cubic crystal system with the space

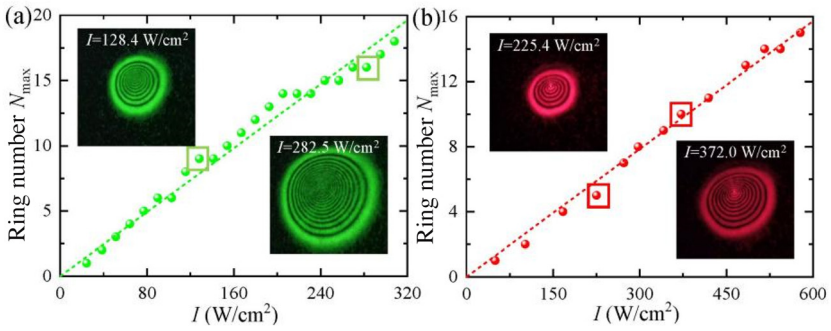


Fig. 3 Intensity dependence of $N_{max}$ for the InP nanosheets at (a) $\lambda$ = 532 nm and (b) 671 nm. The corresponding insets display complete self-diffraction ring patterns at two characteristic intensities.

group $F\bar{4}3m$, the lattice constants obtained from XRD in Fig. 1(c) are $a = b = c = 5.86$ Å. Accordingly, the number of molecules covering a single effective layer is $m = 8.74 \times 10^{14}$. Thus, the effective number of layers for InP nanosheets is estimated to be $N_{\text{eff}} = M/m \approx 224$. In this way, the third-order nonlinear susceptibilities of monolayer InP nanosheets $\chi^{(3)}_{\text{monolayer}}$ are obtained as $(1.28 \pm 0.02) \times 10^{-9}$ esu at $\lambda = 532$ nm and $(7.52 \pm 0.09) \times 10^{-10}$ esu at $\lambda = 671$ nm. By comparison, Table 1 also lists the third-order nonlinear susceptibilities $\chi^{(3)}_{\text{monolayer}}$ of representative 2D nanomaterials. It is shown that the $\chi^{(3)}_{\text{monolayer}}$ values of InP nanosheets are comparable to those of 2D $Ga_2Te_3$[21] and $MoSe_2$ nanoflakes.[34]

The $\chi^{(3)}_{\text{monolayer}}$ value of 2D nanomaterials is correlated to the carrier mobility $\mu$ and the carrier effective mass $m^*$ using the empirical formulas:[39]

$$\chi^{(3)}_{\text{monolayer}} = 0.146 \times \sqrt{\mu}, \quad (3)$$

$$\chi^{(3)}_{\text{monolayer}} = 8.00/\sqrt{m^*}. \quad (4)$$

Fig. 4 shows the correlation between $\chi^{(3)}_{\text{monolayer}}$ and the carrier mobility $\mu$ with the effective mass $m^*$ of InP nanosheets, where $\mu = 4800$ cm$^2$ V$^{-1}$ s$^{-1}$ and $m^* = 0.08 \times m_0$ ($m_0$ is the mass of free electrons), respectively.[7] To provide a clear comparison, Fig. 4 also presents the values of other representative 2D nanomaterials including graphene,[37] black phosphorus (BP),[33] boron,[40] $Ga_2Te_3$,[21] $MoS_2$,[21] $MoSe_2$,[21] and $MoTe_2$.[21]

As observed from the confidence bands (dark-colored area) and prediction bands (light-colored area) in Fig. 4, the relationship between the third-order nonlinear susceptibility $\chi^{(3)}_{\text{monolayer}}$ of monolayer InP nanosheets measured in this work and the carrier mobility $\mu$ or effective mass $m^*$ described by the empirical formula (see eqn (3) or (4)) is basically consistent; its value is positively correlated with the carrier mobility $\mu$ and negatively correlated the with effective mass $m^*$. This consistency not only validates the effectiveness of the wind-chime model in interpreting the electronic coherence of InP nanosheets but also further supports the reliability of our experimental results. Meanwhile, it highlights the potential of InP as a III–V semiconductor for future applications in nonlinear photonic devices.

### 3.6 Nonlinear optical properties of InP suspensions against photodegradation

The long-term stability and resistance to photodegradation of nonlinear optical materials are crucial. Therefore, we repeatedly conducted SSPM measurements on the same sample on different dates to validate the reliability of its nonlinear optical performance. In order to mitigate oxidation of the InP nanosheet dispersion following extended storage, the sample is preserved under ambient conditions at a temperature of 25 °C.

Fig. 5(a) presents the maximum number of self-diffraction rings $N_{\text{max}}$ measured at different intensities $I$ for the same InP nanosheet dispersion after storage durations of 1, 28, and 56 days. The results reveal two main characteristics: (i) for the sample with the same storage duration, $N_{\text{max}}$ increases approximately linearly with the increase of $I$, and (ii) for the sample with different storage durations, the values of $N_{\text{max}}$ show slight variations at the same intensity. For example, the inset in Fig. 5(a) displays the complete self-diffraction ring patterns obtained at an intensity of $I = 308.2$ W cm$^{-2}$ after 1 day, 28 days, and 56 days of storage. It is clearly observed that the measured maximum number of rings decreases from $N_{\text{max}} = 18$ on day 1 to 16 on day 56.

Based on the linear dependence between $N_{\text{max}}$ and $I$ measured over time, as shown in Fig. 5(a), the nonlinear refractive indices $n_2$ of the InP nanosheet dispersions are calculated using eqn (1). The results are presented in Fig. 5(b). As anticipated, the measured $n_2$ values exhibit a slight decrease with prolonged storage time. Specifically, the $n_2$ value decreases from $(1.18 \pm 0.02) \times 10^{-6}$ cm$^2$ W$^{-1}$ on day 1 to $(1.09 \pm 0.02) \times 10^{-6}$ cm$^2$ W$^{-1}$ on day 56, corresponding to a relative reduction of 7.6% in the nonlinear refractive index. In short, Fig. 5 demonstrates that the nonlinear optical performance of the InP nanosheet dispersions remains largely stable, even after more than two months of storage, despite a minor degradation. Furthermore, repeated SSPM measurements confirm the sample's robust resistance to laser-induced degradation. These findings suggest that InP nanosheets, exhibiting long-term stability and high photodegradation resistance (similar to

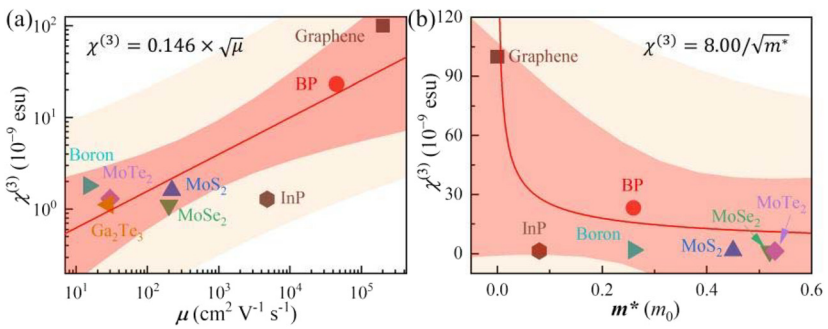


Fig. 4 Correlation between $\chi^{(3)}_{\text{monolayer}}$ and (a) the carrier mobility $\mu$ with (b) the effective mass $m^*$.

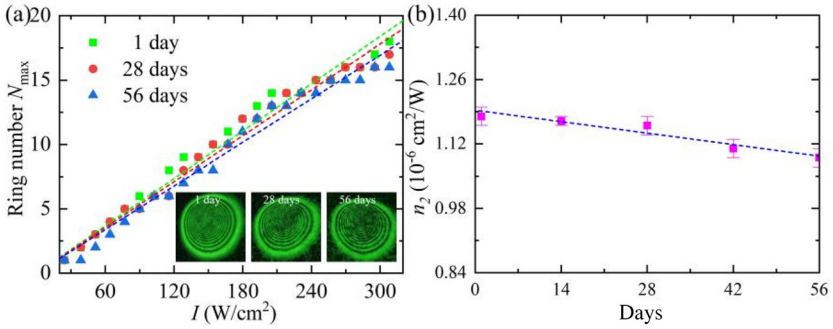


Fig. 5 SSPM experimental results for the InP nanosheet dispersion after different storage days. (a) The maximum ring number $N_{max}$ as a function of intensity $I$ for various storage days. The insets show the complete self-diffraction ring patterns recorded at $I$ = 308.2 W cm$^{-2}$ after 1, 28, and 56 days. (b) The nonlinear refractive indices $n_2$ derived for different storage durations.

few-layer VP,[41] Ag/VP heterojunctions,[42] and MoP microparticles[25]), hold significant promise for applications in nonlinear photonic devices.

## 4 Application of multifunctional nonlinear photonic devices

As presented in Section 3, the InP nanosheets exhibit superior electronic coherence and photostability. Leveraging the excellent SSPM behaviors of InP nanosheet dispersions, we design and demonstrate four types of nonlinear photonic devices, namely an all-optical switch, a spatially asymmetric light transmitter, a photonic diode, and an optical logic gate.

### 4.1 All-optical switches

Utilizing the excellent nonlinear optical properties of InP nanosheets, we construct the all-optical switching setup, as illustrated in Fig. 6(a). A 532 nm control beam is intensity-modulated using a half-wave plate ($\lambda/2$) followed by a G–T prism. This beam is then spatially overlapped with a 671 nm signal beam *via* a beam splitter (BS). Both beams are subsequently focused using a converging lens with a focal length of $f$ = 400 mm onto a quartz cuvette containing a dispersion of InP nanosheets in NMP solvent. The resulting nonlinear interaction produces self-diffraction ring patterns, which are projected onto a white screen or recorded using a camera placed in the far field.

The operating principle of the all-optical switch based on SSPM in the InP nanosheets is as follows. When a strong 532 nm control beam illuminates the sample, it induces a strong nonlinear optical response, generating free carriers that modify the local refractive index. This refractive index change subsequently modulates the phase of the co-propagating weak 671 nm signal beam, leading to self-diffraction effects that manifest as concentric rings. The presence or absence of the 532 nm control beam thus governs whether the 671 nm signal beam can exhibit a multi-ring pattern, constituting the switching action.

Using the experimental setup depicted in Fig. 6(a), the all-optical switching performance of InP nanosheet dispersions is demonstrated in Fig. 6(b). The intensity of the 671 nm signal beam is fixed at $I_s$ = 6.6 W cm$^{-2}$, below its SSPM excitation threshold intensity of $I_{th}^{s}$ = 21.4 W cm$^{-2}$. Initially, the 532 nm control beam is set to $I_c$ = 8.4 W cm$^{-2}$, also below its respective threshold intensity $I_{th}^{c}$ = 19.3 W cm$^{-2}$. At these low intensities, neither beam could generate a self-diffraction ring pattern, and the switch remained in the "off" state (see the first row in Fig. 6(b)). When the control beam intensity is increased to $I_c$ = 138.1 W cm$^{-2}$ (see Fig. 6b④), a green self-diffraction ring emerges, confirming that the control beam alone could excite SSPM. When both the control and signal beams are simultaneously focused onto the sample, distinct green-red self-diffraction rings appear, indicating that the signal beam is phase-modulated *via* the optical nonlinearity induced by the control beam. In this state, both beams contribute to the ring patterns, and the switch is turned "on".

To investigate the dynamic behavior of the all-optical switch, we selected $I_c$ = 256.8 W cm$^{-2}$ of the 532 nm control beam and $I_s$ = 6.6 W cm$^{-2}$ of the 671 nm signal beam. The insets in Fig. 6(c) display the representative self-diffraction ring patterns observed at three distinct time points. Fig. 6(c) illustrates the temporal evolution of the ring number $N_s$ generated by the 671 nm signal beam. Similar to single-beam SSPM dynamics (see Fig. 2(a)), both beams transition over time from a single spot to a multi-ring diffraction pattern. Furthermore, the rings generated by each beam undergo three characteristic stages: formation, collapse, and stabilization. To quantitatively assess the switching performance, we define two key metrics: the switching time $\tau_s$ and the maximum number of signal self-diffraction rings $N_s^{max}$. The switching time $\tau_s$ is defined as the duration from when the 532 nm control beam first interacts with the sample to the moment when a complete self-diffraction ring pattern is formed by the 671 nm signal beam *via* the SSPM effect.

Fig. 6(d) and (e) present the switching time $\tau_s$ and the maximum ring number of the 671 nm signal beam $N_s^{max}$, respectively, as functions of the 532 nm control beam intensity $I_c$. It is observed that $\tau_s$ decreases linearly with increasing $I_c$,

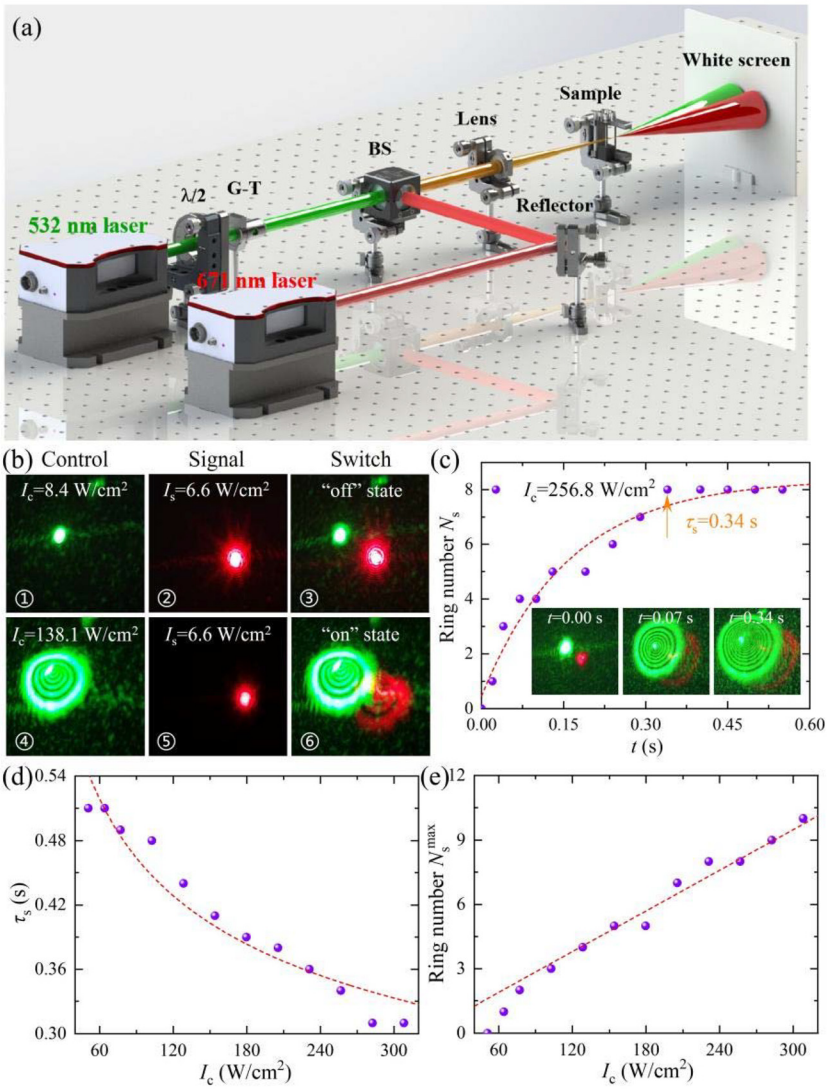


**Fig. 6** All-optical switch based on SSPM in InP nanosheet dispersions. (a) Schematic diagram of the experimental setup. (b) Performance demonstration of the all-optical switching. (c) The evolution of the ring number $N_s$ of 671 nm signal beam over time $t$ at $I_c$ = 256.8 W cm$^{-2}$. The insets are the self-diffraction ring patterns at three typical times. (d) $I_c$-dependent switching time $\tau_s$ and (e) the maximum ring number of the 671 nm signal beam $N_s^{max}$.

while $N_s^{max}$ exhibits a linear increase. This behavior can be attributed to the enhanced optical nonlinearity in the InP nanosheet suspension under stronger control beam illumination. A higher $I_c$ leads to a greater nonlinear refractive index change, which accelerates the formation of the signal self-diffraction rings and results in a higher number of complete rings.

### 4.2 Spatially asymmetric light transmitters

Leveraging the strong SSPM response of InP nanosheets, we construct cascaded samples to investigate spatially asymmetric light propagation. The sample assembly consists of two 10 mm-thick quartz cuvettes placed in sequence, one containing a dispersion of InP nanosheets and the other of GO nanosheets in NMP, each at a mass concentration of 0.127 mg mL$^{-1}$. GO is selected for its compatibility with solution processing and ease of preparation. The laser beam with a wavelength of 532 nm is directed through two distinct configurations: InP followed by GO (denoted as InP/GO) and GO followed by InP (denoted as GO/InP), referred to as the forward and reverse configurations, respectively.

The working principle of spatially asymmetric light propagation based on the SSPM effect is described as follows:[25,43] a cascaded sample is constructed by combining two nonlinear samples with significantly distinct nonlinear refractive indices. When a laser beam propagates through this cascaded assembly in both forward and reverse directions, noticeable differences emerge in both the number of self-diffraction rings and their formation dynamics. It is emphasized that the key distinction between a conventional SSPM experiment and spatially asymmetric light propagation lies in the sample con-

 

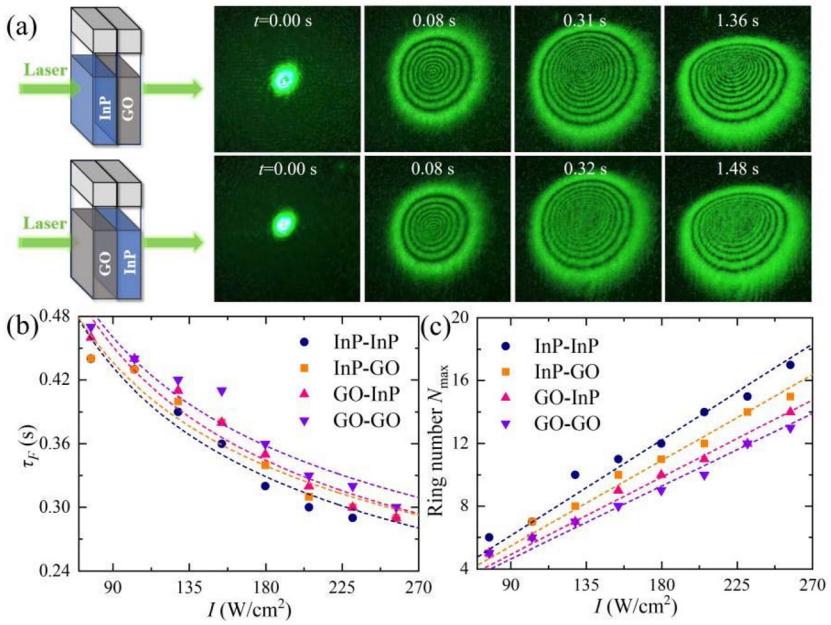


**Fig. 7** Spatially asymmetric light transmitter based on SSPM in InP/GO cascaded samples. (a) The self-diffraction ring patterns observed over time $t$ in InP/GO and GO/InP cascaded samples at $I$ = 205.5 W cm$^{-2}$. (b) Ring formation time $\tau_F$ and (c) maximum ring number $N_{max}$ as a function of intensity $I$ for the InP/InP, InP/GO, GO/InP, and GO/GO cascaded samples.

figuration—the latter employs a cascaded sample rather than a single material.

Fig. 7(a) shows the temporal evolution of self-diffraction rings for both InP/GO and GO/InP configurations at $I$ = 205.5 W cm$^{-2}$. In both propagation directions, the beam evolves from a central spot into a multi-ring diffraction pattern, exhibiting three characteristic stages: formation, collapse, and stabilization. At $I$ = 205.5 W cm$^{-2}$, the measured ring formation times are $\tau_F$ = 0.31 s for InP/GO and 0.32 s for GO/InP, while the maximum numbers of rings are $N_{max}$ = 12 and 11, respectively. These results clearly demonstrate that reversing the beam propagation direction through the cascaded sample leads to distinct nonlinear responses, as reflected in the differences in both $\tau_F$ and $N_{max}$. Thus, spatially asymmetric light propagation is conclusively achieved *via* the SSPM in the InP/GO-cascaded samples.

Fig. 7(a) and (b) present the ring formation time $\tau_F$ and the maximum ring number $N_{max}$ as a function of intensity $I$ for the cascaded InP/GO and GO/InP samples, along with comparative results from the homogeneous InP/InP and GO/GO samples. Similar to the behavior observed in single-material systems (see Fig. 2(c) and 3), both $\tau_F$ and $N_{max}$ exhibit a dependency on intensity $I$ across all four samples: $\tau_F$ decreases nonlinearly with $I$, while $N_{max}$ increases linearly. These results indicate that stronger optical intensities enhance the nonlinear optical response, leading to a higher number of self-diffraction rings and faster nonlinear dynamics. At a fixed intensity $I$, the measured $\tau_F$ values follow the order: GO/GO > GO/InP > InP/GO > InP/InP, while the $N_{max}$ values decrease in the reverse order. This trend arises from the difference in nonlinear refractive indices between the InP nanosheets ($n_2$ = 1.18 × 10$^{-6}$ cm$^2$ W$^{-1}$) and the GO nanosheets ($n_2$ = 9.13 × 10$^{-7}$ cm$^2$ W$^{-1}$). The nonlinear performance of the cascaded samples (InP/GO and GO/InP) lies between those of the two homogeneous samples (InP/InP and GO/GO), resulting in intermediate $\tau_F$ and $N_{max}$ values. Briefly, by leveraging SSPM in the cascaded InP/GO structures, we demonstrate predictable control over ring formation dynamics and the self-diffraction ring number in spatially asymmetric light propagation.

The spatially asymmetric light propagation performance demonstrated in Fig. 7 can be quantitatively evaluated using the nonreciprocity factor $C$, which characterizes the strength of the nonreciprocal nonlinear optical response, as defined by:[43,44]

$$C = \frac{|n_{12} - n_{21}|}{\max(n_{12}, n_{21})} \quad (5)$$

where $n_{12}$ and $n_{21}$ denote the nonlinear refractive indices of the InP/GO and GO/InP cascaded samples, respectively. A smaller value of $C$ corresponds to a weaker nonreciprocal response. Based on the intensity-dependent $N_{max}$ values in Fig. 7(c), the fitted slopes are $s_{12}$ = 0.061 ± 0.001 cm$^2$ W$^{-1}$ for InP/GO and $s_{21}$ = 0.055 ± 0.001 cm$^2$ W$^{-1}$ for GO/InP. Using eqn (1), these correspond to $n_{12}$ = (1.17 ± 0.02) × 10$^{-6}$ cm$^2$ W$^{-1}$ and $n_{21}$ = (1.06 ± 0.02) × 10$^{-6}$ cm$^2$ W$^{-1}$. The resulting value of $C$ is 0.09, which is comparable to previously reported values such as $C$ = 0.098 for $CsPbI_3$ quantum dot/Bi nanosheet systems.[43] This spatially asymmetric light propagation of 2D nanomaterials offers potential for developing nonlinear photonic devices such as photonic diodes,[34] optical logic gates,[40] and optical isolators.[23]

### 4.3 Photonic diodes

Let's examine a limiting case of eqn (5), in which the cascaded sample enables the excitation of SSPM under the forward configuration but completely suppresses it under the reverse configuration. Under these conditions, the nonreciprocity factor reaches $C = 1$. This behavior is analogous to the unidirectional current conduction in an electronic diode, thereby constituting a "photonic diode" mechanism that achieves spatially asymmetric light propagation—*i.e.*, optical nonreciprocity.

To validate this concept, we design an SSPM experiment based on an InP/$SnS_2$ cascaded sample, leveraging the strong nonlinear refraction of InP nanosheets and the reverse saturable absorption of $SnS_2$ nanosheets. Dispersions of InP and $SnS_2$ nanosheets in NMP solvent—each at a mass concentration of 0.032 mg $mL^{-1}$—are prepared and housed in two separate 10 mm-thick quartz cuvettes. These cuvettes are arranged side-by-side to form the cascaded sample, as schematically illustrated in Fig. 8(a). In the experimental setup, a laser beam with a wavelength of 532 nm is used. The forward configuration is defined as the beam traversing through the InP sample first and then the $SnS_2$ sample, while the reverse configuration refers to the beam first passing through $SnS_2$ and then InP.

Fig. 8(a) displays the self-diffraction ring patterns of the cascaded sample at $\lambda = 532$ nm at different intensities $I$, with the laser beam passing through the structure in both the forward (InP/$SnS_2$) and reverse ($SnS_2$/InP) directions. The results show that multiple concentric self-diffraction rings are observed when light travels in the forward direction through the diode. In contrast, no diffraction rings are generated under reverse illumination, demonstrating the photonic diode functionality using the InP/$SnS_2$ cascaded sample.

Quantitatively, Fig. 8(b) presents the intensity-dependent maximum number of self-diffraction rings $N_{max}$ generated by the photonic diode. When the beam passes through the cascaded sample in the forward direction (InP/$SnS_2$), the laser first interacts with the InP dispersion, which exhibits strong nonlinear refraction, efficiently exciting self-diffraction rings. As the light subsequently traverses the $SnS_2$ dispersion, the number of rings remains unchanged; however, the intensity of the SSPM rings is reduced due to the absorption behavior of $SnS_2$. Conversely, when the laser beam enters from the reverse direction ($SnS_2$/InP), it first passes through the $SnS_2$ dispersion. Owing to the large optical bandgap of $SnS_2$ ($E_g$ = 2.6 eV (ref. 45)), the laser beam with a photon energy of $h\nu$ = 2.33 eV does not interact significantly with $SnS_2$. It is noteworthy that the reverse saturable absorption behavior of $SnS_2$ greatly attenuates the incident laser power,[46] making it difficult to excite diffraction rings. Meanwhile, the reduced intensity of the light reaching the InP dispersion is insufficient to exceed the threshold for generating self-diffraction rings, as confirmed by the red curve in Fig. 8(b). Through the experimental verification shown in Fig. 8, we demonstrate that a photonic diode based on the InP/$SnS_2$ cascaded sample can easily achieve asymmetric light propagation for the nonreciprocity factor $C = 1$, showing promising potential for applications in all-optical information processing.

### 4.4 Optical logic gates

Benefiting from their excellent laser-induced electronic coherence and high photostability, the InP nanosheets are promising not only for photonic diodes but also for all-optical OR logic gates. In such a logic device, a stronger laser beam modulates the propagation of a weaker one, mimicking the behavior of electronic OR gates. The logic states are defined based on optical intensity: low- and high-power levels in the input laser beams are assigned to logic "0" and "1", respectively. The output is considered "1" whenever self-diffraction rings are generated; otherwise, the output remains "0".

In the optical OR gate, the system comprises two inputs—"A" (Laser A) and "B" (Laser B)—as shown in Fig. 9(a) and (b), and a single output "Y" (where Y = A + B). The output "Y" attains a high logic level "1" if at least one of the inputs "A" or "B" is at the high level "1". Conversely, only when both "A" and "B" are at the low logic level "0", the output "Y" remains at "0". These results are consistent with the waveform depicted in Fig. 9(c).

The optical logic gate shares similarities with the all-optical switch described in Subsection 4.1, as both employ two laser beams with different photon energies. However, unlike the all-optical switch, where the control and signal beams are strictly defined, the two beams in the logic gate are mutually modulatable and interchangeable, with adjustable intensities. In our

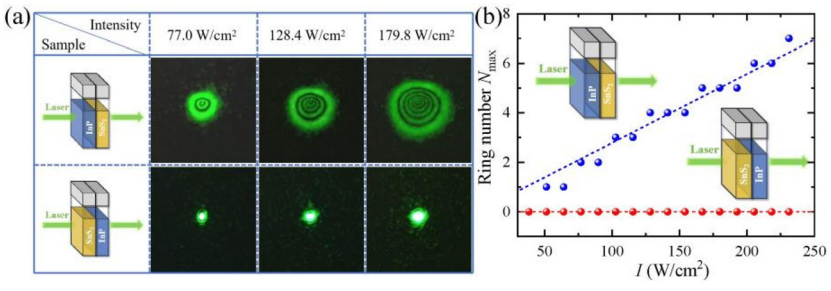


Fig. 8 Photonic diode based on SSPM in the InP/$SnS_2$ cascaded samples. (a) Self-diffraction ring patterns of the cascaded samples at different $I$ at $\lambda$ = 532 nm when the laser beam passes through the forward (InP/$SnS_2$) and reverse ($SnS_2$/InP) directions. (b) Intensity-dependent maximum ring number $N_{max}$ for the photonic diode.

 

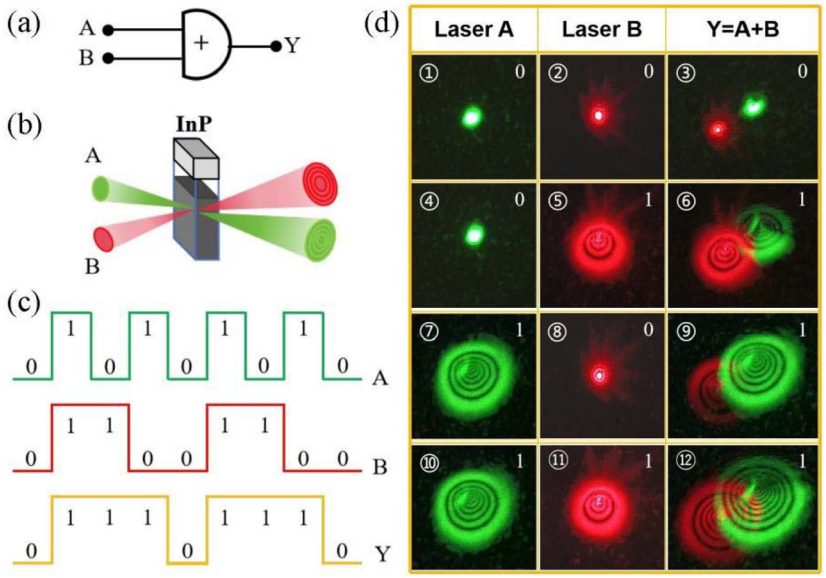


**Fig. 9** All-optical logic gates based on InP nanosheet dispersions. (a) Symbol of the logical OR gate. (b) Schematic diagram of the optical modulation system. (c) Input and output waveforms for the OR logic operation. (d) Experimental results of the logic OR gate at $\lambda$ = 532 nm and 671 nm.

experiments, two laser beams with wavelengths of $\lambda$ = 532 nm and 671 nm are incident on the InP nanosheet dispersion, and the resulting self-diffraction rings serve as the input optical signals. When both input beams "A" and "B" are at a low intensity level ("0"), they do not interact sufficiently with the sample due to their low intensity, failing to produce any SSPM rings on the far-field screen (see Fig. 9d①–③). If Laser A remains at "0" while Laser B is increased to a high intensity ("1"), the output "Y" switches to a high level ("1"), consistent with the OR logic operation "0 + 1 = 1". As shown in Fig. 9d④–⑥, when the high-intensity red laser beam passes through the InP nanosheet dispersion, it modifies the spatial refractive index distribution of the medium, inducing an additional nonlinear phase shift. This change subsequently enables the cross-coupled weaker beam (Laser B) to generate self-diffraction ring patterns. Conversely, the stronger beam (Laser A) can also modulate the weaker beam (Laser B), as shown in Fig. 9d⑦–⑨. Similarly, when both beams are at high intensity (logic "1"), clearly visible self-diffraction rings with larger diameters are observed, consistent with the results presented in Fig. 9d⑩–⑪. In a word, the output measurements under the four states illustrated in Fig. 9d demonstrate the successful implementation of an all-optical OR logic gate, confirming the feasibility of performing logic operations purely through optical control without intermediate electronic conversion.

## 5 Conclusions

In summary, we have prepared and characterized InP nanosheet dispersions, investigated their SSPM behaviors, and demonstrated their applications in multifunctional nonlinear photonic devices. Through analysis of the dynamics of self-diffraction ring formation, the ring formation time $\tau_F$ and the third-order nonlinear susceptibility of monolayer InP nanosheets $\chi^{(3)}_{monolayer}$ are determined to be approximately 0.3 s and $10^{-9}$ esu, respectively—values comparable to those of typical 2D nanomaterials. The dominant mechanism underlying the light–InP interactions in the SSPM is laser-induced electron coherence, with the thermal effect playing a secondary role. Repeated tests conducted on samples aged nearly two months confirm that their nonlinear optical response remains generally stable, indicating good photophysical stability of the InP nanosheets. Leveraging the superior electronic coherence and photostability of InP nanosheets, we have designed and demonstrated four types of nonlinear photonic devices: all-optical switches using InP nanosheets, spatially asymmetric light transmitters based on the InP/GO cascaded structure, photonic diodes employing InP/$SnS_2$ cascaded systems, and optical logic gates utilizing InP nanosheets. This work not only addresses a significant gap in the third-order nonlinear optical research of III–V semiconductor nanomaterials, but also opens new pathways for developing high-performance multifunctional nonlinear photonic devices. Finally, the following remarks are made on the multifunctional nonlinear photonic devices based on SSPM in InP nanosheets: the advantages include a simple device structure, no need for external electronic modulation, and ease of fabrication; the drawback lies in the sub-second-scale ring formation time due to the wind-chime-like reorientation of InP nanosheets under an external field, which leads to a relatively slow response of these devices.

## Conflicts of interest

There are no conflicts to declare.

## Data availability

The data related to this study are included in the article. The author ensures that the data presented in the article are accurate and reliable. Any additional data are made available from the corresponding author on reasonable request.

## Acknowledgements

This work was supported by the National Natural Science Foundation of China (Grant No. 12474323 and 12074066).

## References

1 J. A. del Alamo, *Nature*, 2011, **479**, 317–323.
2 Y. Zhu, V. Raj, Z. Li, H. H. Tan, C. Jagadish and L. Fu, *Adv. Mater.*, 2021, **33**, 2105729.
3 H. Wang, D. Zhou, R. Zhang, D. Lu, L. Zhao, H. Zhu, W. Wang and C. Ji, *Chin. Phys. Lett.*, 2015, **32**, 084203.
4 S. Mokkapati and C. Jagadish, *Mater. Today*, 2009, **12**, 22–32.
5 X. Wang, L. Xu, Y. Jiang, Z. Yin, C. C. S. Chan, C. Deng and R. A. Taylor, *J. Semicond.*, 2019, **40**, 071906.
6 J. Liu, H. Nie, B. Yan, K. Yang, H. Yang, V. Khayrudinov, H. Lipsanen, B. Zhang and J. He, *Photonics Res.*, 2020, **8**, 1035–1041.
7 W. Walukiewicz, J. Lagowski, L. Jastrzebski, P. Rava, M. Lichtensteiger, C. H. Gatos and H. C. Gatos, *J. Appl. Phys.*, 1980, **51**, 2659–2668.
8 C. Jacoboni, C. Canali, G. Ottaviani and A. A. Quaranta, *Solid-State Electron.*, 1977, **20**, 77–89.
9 G. Chen, M. Wang, W. Yang, M. Tan, Y. Wu, P. Dai, Y. Huang and S. Lu, *J. Semicond.*, 2017, **38**, 124004.
10 V. Jain, M. Heurlin, E. Barrigon, L. Bosco, A. Nowzari, S. Shroff, V. Boix, M. Karimi, R. J. Jam, A. Berg, L. Samuelson, M. T. Borgström, F. Capasso and H. Pettersson, *ACS Photonics*, 2017, **4**, 2693–2698.
11 Y. Zhang, Y. Ji, A. Khaliq, H. Chai, M. Ali, A. Qadir, I. Saeed, X.-G. Yang and S. Du, *Appl. Phys. A:Mater. Sci. Process.*, 2024, **130**, 531.
12 M. D. Dvorak and B. L. Justus, *Opt. Commun.*, 1995, **114**, 147–150.
13 H. Wang, D. Wang, G. Chen and H. Liu, *Chin. Phys. Lett.*, 2007, **24**, 2600–2602.
14 Y. Wu, Q. Wu, F. Sun, C. Cheng, S. Meng and J. Zhao, *Proc. Natl. Acad. Sci. U. S. A.*, 2015, **112**, 11800–11805.
15 Y. Liao, C. Song, Y. Xiang and X. Dai, *Ann. Phys.*, 2020, **532**, 2000322.
16 L. Wu, X. Yuan, D. Ma, Y. Zhang, W. Huang, Y. Ge, Y. Song, Y. Xiang, J. Li and H. Zhang, *Small*, 2020, **16**, 2002252.
17 Y. Gao, Y. Hu, C. Ling, G. Rui, J. He and B. Gu, *Nanoscale*, 2023, **15**, 6225–6233.
18 L. Wu, Z. Xie, L. Lu, J. Zhao, Y. Wang, X. Jiang, Y. Ge, F. Zhang, S. Lu, Z. Guo, J. Liu, Y. Xiang, S. Xu, J. Li, D. Fan and H. Zhang, *Adv. Opt. Mater.*, 2018, **6**, 1700985.
19 Y. Shan, J. Tang, L. Wu, S. Lu, X. Dai and Y. Xiang, *J. Alloys Compd.*, 2019, **771**, 900–904.
20 L. Wu, X. Jiang, J. Zhao, W. Liang, Z. Li, W. Huang, Z. Lin, Y. Wang, F. Zhang, S. Lu, Y. Xiang, S. Xu, J. Li and H. Zhang, *Laser Photonics Rev.*, 2018, **12**, 1800215.
21 A. Pramanik, P. Kumbhakar, A. Dey, K. Mondal, D. Banerjee, V. R. Soma, P. Kumbhakar and C. S. Tiwary, *ACS Appl. Opt. Mater.*, 2023, **1**, 1634–1642.
22 L. Wu, W. Huang, Y. Wang, J. Zhao, D. Ma, Y. Xiang, J. Li, J. S. Ponraj, S. C. Dhanabalan and H. Zhang, *Adv. Funct. Mater.*, 2019, **29**, 1806346.
23 L. Wu, Y. Zhang, X. Yuan, F. Zhang, W. Huang, D. Ma, J. Zhao, Y. Wang, Y. Ge, H. Huang, N. Xu, J. Kang, Y. Xiang, Y. Zhang, J. Li and H. Zhang, *Appl. Mater. Today*, 2020, **19**, 100589.
24 J. Xu, C. Zhang, Y. Wang, M. Wang, Y. Xu, T. Wei, Z. Xie, S. Liu, C.-K. Lee, X. Hu, G. Zhao, X. Lv, H. Zhang, S. Zhu and L. Zhou, *Nat. Commun.*, 2024, **15**, 1726.
25 D. Weng, C. Ling, Y. Gao, G. Rui, L. Fan, Q. Cui, C. Xu and B. Gu, *Laser Photonics Rev.*, 2025, **19**, 2401587.
26 S. K. Nayak, M. S. Ahmed, R. Murali, B. Bhavani, S. Prasanthkumar, L. Giribabu and S. S. K. Raavi, *J. Mater. Chem. C*, 2024, **12**, 9841–9852.
27 A. Ciesielski and P. Samorì, *Chem. Soc. Rev.*, 2014, **43**, 381–398.
28 P. Huang, X. Liu, G. Jin, F. Liu, H. Shen and H. Li, *Adv. Opt. Mater.*, 2023, **11**, 2300612.
29 Y. Niu, S. Ma, H. Dong, Z. Yang, X. Hao, B. Han, S. Wu, H. Dong and B. Xu, *Chin. J. Lumin.*, 2024, **45**, 779–793.
30 J. Tauc, R. Grigorovici and A. Vancu, *Phys. Status Solidi*, 1966, **15**, 627–637.
31 T. Davarzani, A. Bakhshayeshi, I. Motie and R. Taghavimendi, *Physica E*, 2023, **147**, 115599.
32 H. Sahin, S. Cahangirov, M. Topsakal, E. Bekaroglu, E. Akturk, R. T. Senger and S. Ciraci, *Phys. Rev. B: Condens. Matter Mater. Phys.*, 2009, **80**, 155453.
33 X. Xu, M. Wang, Y. Zhang, Q. Li, W. Niu, Y. Yang, J. Zhao and Y. Wu, *Laser Photonics Rev.*, 2024, **18**, 2300930.
34 K. Sk, B. Das, N. Chakraborty, M. Samanta, S. Bera, A. Bera, D. S. Roy, S. K. Pradhan, K. K. Chattopadhyay and M. Mondal, *Adv. Opt. Mater.*, 2022, **10**, 2200791.
35 J. N. Heyman, D. Bell and T. Khumalo, *Appl. Phys. Lett.*, 2006, **88**, 162104.
36 S. D. Durbin, S. M. Arakelian and Y. R. Shen, *Opt. Lett.*, 1981, **6**, 411–413.
37 R. Wu, Y. Zhang, S. Yan, F. Bian, W. Wang, X. Bai, X. Lu, J. Zhao and E. Wang, *Nano Lett.*, 2011, **11**, 5159–5164.
38 Y. Liao, Y. Shan, L. Wu, Y. Xiang and X. Dai, *Adv. Opt. Mater.*, 2020, **8**, 1901862.
39 L. Hu, F. Sun, H. Zhao and J. Zhao, *Opt. Lett.*, 2019, **44**, 5214–5217.
40 C. Song, Y. Liao, Y. Xiang and X. Dai, *Sci. Bull.*, 2020, **65**, 1030–1038.

 

41 L. Zhou, J. Kang, Y. Dong, Y. Wang, Y. Li, H. Huang, S. Xiao, Y. Wang and J. He, *Nano Res.*, 2023, **16**, 5843–5849.
42 Y. Gao, C. Ling, D. Weng, G. Rui, J. He, Q. Cui, C. Xu and B. Gu, *Nanoscale*, 2024, **16**, 18046–18055.
43 L. Wu, K. Chen, W. Huang, Z. Lin, J. Zhao, X. Jiang, Y. Ge, F. Zhang, Q. Xiao, Z. Guo, Y. Xiang, J. Li, Q. Bao and H. Zhang, *Adv. Opt. Mater.*, 2018, **6**, 1800400.
44 L. Wu, Y. Dong, J. Zhao, D. Ma, W. Huang, Y. Zhang, Y. Wang, X. Jiang, Y. Xiang, J. Li, Y. Feng, J. Xu and H. Zhang, *Adv. Mater.*, 2019, **31**, 1807981.
45 G. L. Ye, Y. J. Gong, S. D. Lei, Y. M. He, B. Li, X. Zhang, Z. H. Jin, L. L. Dong, J. Lou, R. Vajtai, W. Zhou and P. M. Ajayan, *Nano Res.*, 2017, **10**, 2386–2394.
46 J. Wu, Y. Tao, X. Wu and Y. Chun, *J. Alloys Compd.*, 2017, **713**, 38–45.